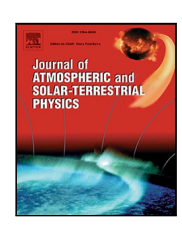


Contents lists available at ScienceDirect

Journal of Atmospheric and Solar–Terrestrial Physics

journal homepage: www.elsevier.com/locate/jastp



Research paper

ULF waves observed in solar wind and on the ground at high, mid, and low latitudes



Embry-Riddle Aeronautical University, Physical Sciences Department, Daytona Beach, FL, 32114-3900, USA



Keywords:
ULF waves
High, middle, low latitudes
Solar wind
Cross-correlation
Ring current
Field line resonator
Dst index



We analyze fluctuations of the magnetic field in the solar wind registered by the ACE satellite in the L1 Lagrangian point and the ULF waves observed with ground magnetometers at high, middle, and low latitudes during 84 intense substorm events. Our goal is to establish possible connections between ULF oscillations observed simultaneously in the different parts of the solar wind–magnetosphere–ionosphere system during substorms. Our analysis reveals that there is a good correlation between oscillations with frequencies less than 1 mHz observed in the solar wind and in three different latitudes during strong substorms. In particular, we show that: (1) the dominant frequencies of the waves observed on the ground at high, middle, and low latitudes are approximately the same; (2) the waves with frequencies of 0.45–0.55 mHz, and 0.75–0.80 mHz are the most often seen in high, middle, and low latitudes and in the solar wind. Therefore, we conclude that there is a strong coupling between the Earth's magnetosphere–ionosphere system and the solar wind in the frequency range below 1 mHz mediated by the disturbances in the magnetic field.

1. Introduction

ULF electromagnetic waves and field-aligned currents are important participants in the exchange of energy, mass, and momentum between the solar wind and the magnetosphere-ionosphere system of the Earth, particularly during substorms. This importance is emphasized in a number of recent studies, e.g. Nykyri et al. (2006), Shprits et al. (2013), Turner et al. (2014), Boyd et al. (2014), Foster et al. (2014b,a), Mann et al. (2016), Moore et al. (2016), Verkhoglyadova et al. (2016), Li et al. (2017), Zou et al. (2017) and Takahashi et al. (2018). Many of these studies show that the power of electromagnetic oscillations observed with ground magnetometers in the auroral and subauroral zone during substorms predominantly maximizes in the frequency range below 1 mHz (e.g. Takahashi et al., 2001; Mishin et al., 2002; Mann et al., 2004; Rae et al., 2012). Such a low frequency suggests that these oscillations are driven by some large-scale driver, possibly located beyond the Earth's inner magnetosphere. There are many hypotheses explaining the origin of the ULF waves in the magnetosphere, such as reconnection in the magneto tail (Angelopoulos et al., 2002), processes related to magnetosphere-ionosphere interactions (Russell et al., 2013), magnetic field line resonances (Samson et al., 1992a,b), Kelvin-Helmholtz type of instabilities on the magnetopause or on the flanks of the magnetosphere (Galinsky and Sonnerup, 1994; Marin et al., 2014), and energetic electron injections (Pilipenko et al., 2002). The most natural driver with such large spatial scales appears to be fluctuations of the magnetic field and plasma pressure in the solar wind. And one of the first ideas in studying ULF waves at high latitudes was establishing a correlation between the fluctuation of the parameters of the solar wind and the oscillations of the magnetic field on the ground. Studies by Kepko and Spence (2001), Kepko et al. (2002), Viall et al. (2009), Guido et al. (2014) and Alimaganbetov and Streltsov (2018) demonstrate that, indeed, there is a correlation between ULF waves detected at high latitudes on the ground, in the inner magnetosphere, and in the solar wind. The dominant frequencies of these fluctuations are in the range 0.60–0.75 mHz.

The main focus of studies on ULF waves is the physical mechanism causing waves with such a low frequency. Two major hypotheses about the origin of these waves include (1) the idea that they are produced by some resonance mechanism inside the magnetosphere and (2) the suggestion that they are directly driven by the oscillations in the dynamic plasma pressure or the magnetic field carried by the solar wind. The main argument supporting the first suggestion is that ULF waves observed at high latitudes with ground magnetometers and radars often have very specific, discrete set of frequencies, highly suggestive that these frequencies are the eigenfrequencies of some resonator cavity in the Earth's magnetosphere–ionosphere system. The well-known example of such frequencies are the so-called "magic" frequencies reported by Samson et al. (1992a,b), and Fenrich et al.

E-mail addresses: alimagam@my.erau.edu (M. Alimaganbetov), streltsa@erau.edu (A.V. Streltsov).

^{*} Corresponding author.

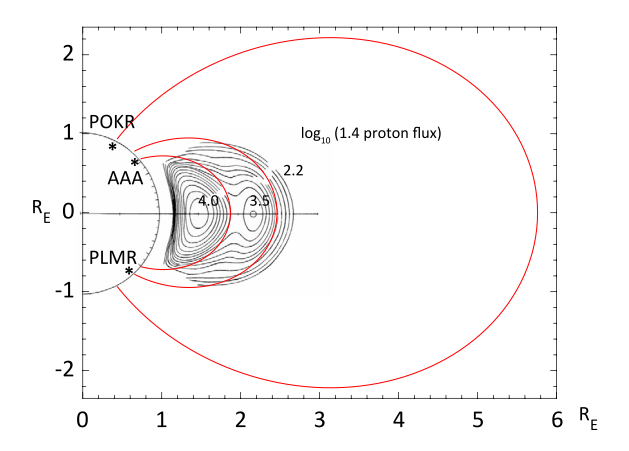


Fig. 1. L-shells of the Earth's magnetic field for (1) Poker Flat station (L = 5.76); (2) Palmer station (L = 2.46); and (3) Alma Ata station (L = 1.87). Isolines show distribution of energetic protons in the inner magnetosphere. *Source:* Adapted from Cravens (1997).

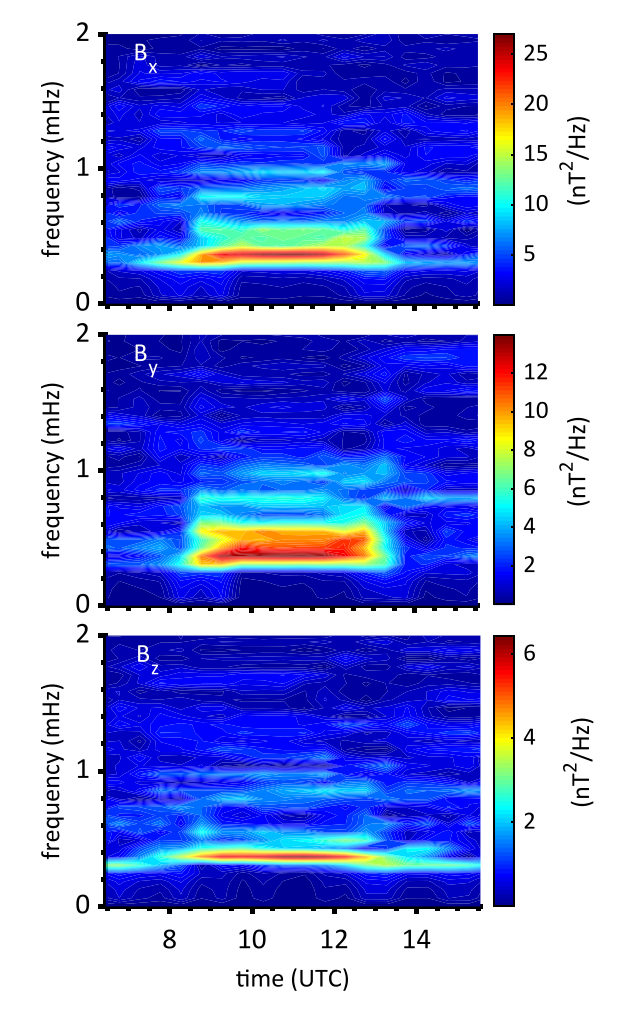


Fig. 2. Spectrograms of B_x , B_y , and B_z components of the magnetic field detected at AAA station during the 05/02/2017 substorm.

(1995), who explained them as the eigenfrequencies of the global magnetospheric resonator formed by the entire closed magnetic flux tube bounded by the ionosphere (Cummings et al., 1969).

This resonator can be driven by fast magnetosonic waves traveling across ambient magnetic field from the reconnection side in the magneto tail (Angelopoulos et al., 2002), or from the flanks of the

magnetopause (the so-called low-latitude boundary layers), where they can be generated by the Kelvin–Helmholtz instabilities driven by the interactions of the solar wind with the Earth's magnetosphere (Galinsky and Sonnerup, 1994; Marin et al., 2014). Standing waves inside the resonator also can be generated by the active magnetosphere-ionosphere interactions (Atkinson, 1970; Sato, 1978; Trakhtengertz and Feldstein, 1984; Miura, 1996). The global resonator can be used for the explanation of ULF waves with frequencies greater than 3–5 mHz, but it is hard to make its eigenfrequency less than 1 mHz without assuming a relatively large density of heavy ions in the magnetosphere, or without extending the field lines far in the tail.

These arguments support the hypothesis that ULF waves with frequencies less than 1 mHz can be produced by the oscillations in the dynamic plasma pressure or the magnetic field carried by the solar wind (Kepko et al., 2002; Viall et al., 2009). They also agree with the results reported by Mishin et al. (2002) that stated: "ULF perturbations in solar wind dynamic pressure and IMF are shown to contribute to the ULF perturbations at high and middle latitudes", meaning that the solar wind serves as a direct driver of these waves in the Earth's magnetosphere. Recently, Alimaganbetov and Streltsov (2018) analyzed ULF waves detected during substorms in the solar wind and at high latitudes on the ground. They analyzed data measured by the NASA ACE satellite dwelling in the L1 Lagrangian point $(1.5 \times 10^6 \text{ km upstream in the})$ solar wind), and the ground magnetometer located at the Poker Flat station (POKR, Mlat = 65.38° , L = 5.76). Their analysis shows that (1) the dominant frequencies of the waves observed on the ground at high latitude and in the solar wind matched in ~30% of all analyzed events, (2) the waves with frequencies of 0.60 mHz and 0.70-0.75 mHz are most often seen at high latitudes and in the solar wind. Therefore, they conclude that there is a strong coupling between the high-latitude part of the Earth's magnetosphere-ionosphere system and the solar wind in the frequency range below 1 mHz. The additional argument supporting the idea of the global magnetosphere-ionosphere resonator coming from that study is the fact that sometimes the ULF waves have been observed on the ground without any correlating disturbances in the solar wind.

The goal of this paper is to analyze 84 intense substorm events published/investigated in the literature and establish a correlation between the ULF fluctuations of the magnetic field observed in the solar wind and the ground magnetometers at middle and low latitudes. This analysis will use the same approach as the one employed by Alimaganbetov and Streltsov (2018).

2. Data sources and analysis methods

We use the magnetic field data provided by the NASA Advanced Composite Explorer (ACE) satellite dwelling in the Earth's L1 Lagrangian point (sampling rate 1 s), and the ground magnetometers located at the high-latitude Poker Flat station in Alaska (POKR, Mlat = 65.38° , L=5.76, sampling rate 1 s), the mid-latitude Palmer station in Antarctica (PLMR, Mlat = -50.40° , L=2.46, sampling rate 0.5 s), and the low-latitude Alma Ata station in Kazakhstan (AAA, Mlat = 43.06° , L=1.87, sampling rate 60 s). These stations are shown in Fig. 1 adapted from Cravens (1997).

Each of these sources provides three components of the magnetic field, and the first task of data analysis is to identify the most "representative" component for every source. For example, Fig. 2 shows spectrograms of the de-trended B_x , B_y , and B_z components of the magnetic field measured at AAA station during the 05/02/2017 substorm. It shows that (1) the power of all three signals reaches its maximum at almost the same frequency of 0.4–0.5 mHz, and (2) the magnitude of the wave disturbance in B_x is substantially larger than the magnitude of B_y and B_z . This finding gives us a rationale to use the B_x component as the most "representative" part of the magnetic signal measured at AAA station. In full analogy, we identify B_H , B_x , and B_y as the most "representative" components of the field measured at POKR, PLMR, and

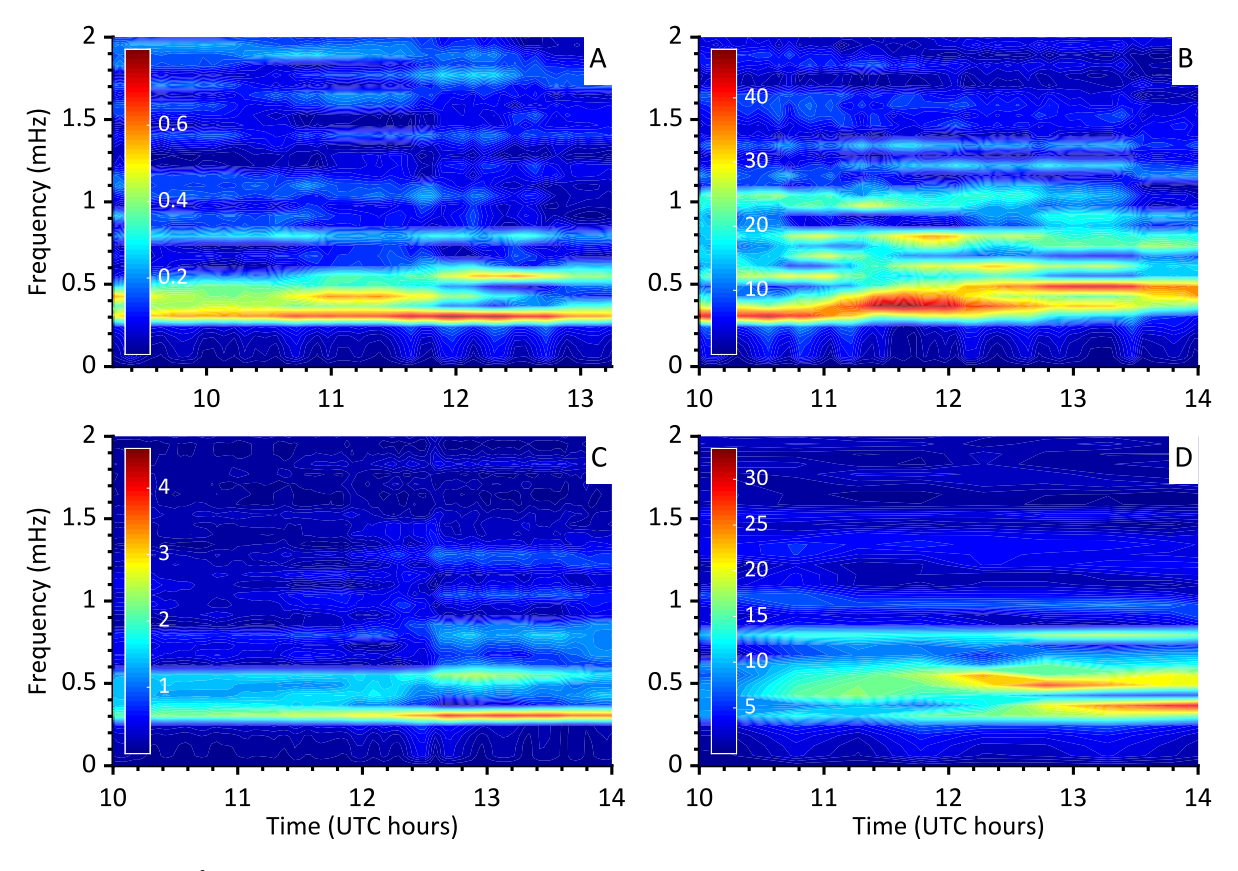


Fig. 3. Power Spectral Density (nT^2/Hz) in all 4 data sources on October 2, 2016, of: (A) B_Y on ACE satellite (shifted by 0.75 UTC relative to the time of ground measurements according to the solar wind speed, 530 km/s); (B) B_H on Poker Flat station; (C) B_X on Palmer station; (D) B_X on Alma Ata station.

ACE, correspondingly. Similar approach was applied in studies of Guido et al. (2014) and Streltsov et al. (2010).

To establish a connection between ULF waves from different sources, we consider two features of these waves. The first feature is the dominant frequency, which is the frequency where the power spectral density (PSD) of the signal reaches its maximum. The second feature is the cross-correlation between signals from different sources, determined by the correlation coefficient, r.

The first step in data analysis includes de-trending of the signals by removing a low-frequency part of the signal by the high-pass filter with a cut-off frequency 0.3 mHz. The exact value of the cut-off frequency for all considered data is chosen carefully after analysis of the PSD of that signal. Also, the filter is applied to the signal which is longer than the considered event and includes the interval of interest in the middle. For example, if an analyzed substorm normally occurs during a twohour time interval, the filter is applied to the signal which is 9.10 h long and contains the substorm event in the middle. Then, the PSD is obtained over a smaller, 4.55 h, window centered on the substorm. This approach allows us to avoid any artificial disturbances of the signal associated with a non-periodicity of the real geomagnetic signals which are, normally, occurring near the signal's ends. The ultimate goad of this filtering is to obtain a signal which most accurately represents the wave oscillations, with no artificial peaks or Gibbs phenomenon, as described by Guido et al. (2014) and Alimaganbetov and Streltsov (2018).

The PSD of the de-trended signal allows us to identify the non-artificial dominant frequency in the signal and to establish if the same frequency is observed in the signals from different sources during the same event. The non-artificial dominant frequency is one that has the second greatest magnitude after the peak near the signal's beginning. We apply the Discrete Fourier Transform to considered signals. The window width is chosen in such a way that it fits only one distinct wave associated with a substorm. We use 4.55 h window, which gives the

frequency resolution of about 0.06 mHz. Fig. 3 shows power spectral density (PSD) plots for the detrended magnetic field measured from all four sources on October 2, 2016. The time of the data from the ACE satellite is shifted by 0.75 UTC relative to the time of ground measurements according to the solar wind speed (530 km/s) detected on ACE during that particular time interval. It shows that all four PSD plots have large magnitudes at frequencies around 0.30–0.50 mHz as well as 0.80 mHz around 1230–1300 UTC on the ground. This feature suggests that the ULF waves detected on the ACE satellite and on three ground stations at 3 different latitudes relate to the same event.

Fig. 4A shows with a red line the Y-component of the magnetic field measured by the ACE satellite on October 2, 2016. The trend of the signal is shown in this figure with the black line. The higher-frequency part of the signal containing the information about ULF waves is shown in Fig. 4B. It is obtained by subtracting the trend from the original signal in the time domain. Fig. 4C shows the PSD of the detrended signal obtained in a 4.55-h window (shaded area on Fig. 4B).

The same procedure is applied to the magnetic field measured by the ground stations. Results of this analysis of the data from all four sources during the October 2, 2016, substorm event are shown in Fig. 4. The PSD plots in this figure demonstrate that all four sources have the same frequency of \sim 0.80 mHz represented as a peak.

To provide some quantitative measure of the similarity between signals from different sources, we calculate the normalized cross-correlation coefficient, r. The cross-correlation is defined as a convolution of two sets of signals x_n , y_n :

$$r_{xy}[m] = \begin{cases} \frac{1}{c_{norm}} \sum_{n=0}^{N-m-1} x_{n+m} y_n^*, \ m \geq 0, \\ r_{yx}[-m], \ m < 0, \end{cases}$$

where m is lag, N is the maximum length of the signal, n is current element, c_{norm} is the normalization coefficient defined as $c_{norm} = \sqrt{(\sum x_n^2 \sum y_n^2)}$. We choose a two-hour window centered around the

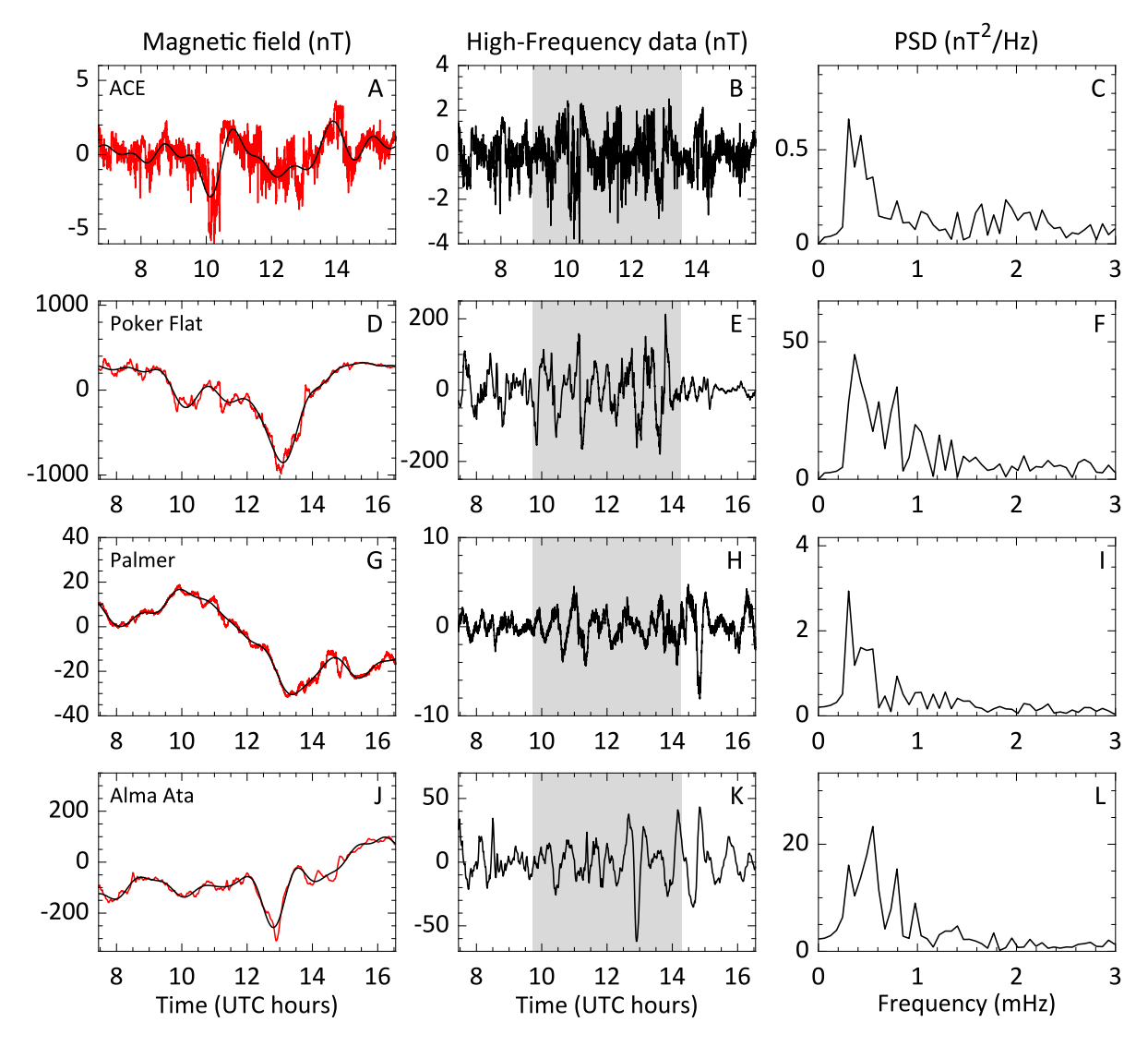


Fig. 4. Substorm event on October 2, 2016. (A) B_Y measured on ACE satellite. A red line is the measured magnetic field, and a black line is its trend. ACE data is shifted by 0.75 UTC according to the solar wind speed. (B) High-frequency part (f > 0.30 mHz) of B_Y on ACE satellite. Shaded region indicates substorm time. (C) Power Spectral Density (PSD) of data in panel (B) over 4 h period. (D) B_H measured on Poker Flat station. A red line is the measured magnetic field, and a black line is its trend. (E) High-frequency part of B_H on Poker Flat station. A red line is the measured magnetic field, and a black line is its trend. (H) High-frequency part of B_X on Palmer station. (I) PSD of data in panel (H) over 4 h period. (J) B_X measured on Alma Ata station. A red line is the measured magnetic field, and a black line is its trend. (K) High-frequency part of B_X on Alma Ata station. (L) PSD of data in panel (K) over 4 h period.

time of the maximum substorm disturbance and compare the signals from all four sources with each other in pairs. Four different combinations are considered: the ACE satellite and the high-latitude POKR station (ACE-POKR); the low-latitude and mid-latitude stations (AAA-PLMR); the high-latitude and mid-latitude stations (POKR-PLMR); and the low-latitude and high-latitude stations (AAA-POKR).

Fig. 5 shows the plot of the cross-correlation coefficient, r, of AAA and PLMR data on March 27, 2017. Panel A shows the comparison of the two signals in the time domain with the largest substorm disturbance at 1045 UTC. It shows that the two signals match each other almost perfectly around the hours of 9.50, 10.00, and 10.75 UTC, having a small shift of about 0.1 h. Panel B shows the plot of cross-correlation coefficients as a function of the lag time. The x-axis in Panel A represents the real time coordinate. The x-axis in Panel B represents a shift of the PLMR signal relative to the AAA signal. A lag time of zero represents a case when both signals are plotted in the same figure against their original time coordinate (exactly as depicted in Panel A). For example, the cross-correlation coefficient of these two signals at zero lag time is about 0.91. As seen in Fig. 5B, the cross-correlation coefficient is almost periodic in time, which implies that these two

signals are of similar frequency. In other words, these two waves should have the same period since their periodically matching crests and troughs result into repetitive high amplitudes of cross-correlation.

While the cross-correlation technique is quantitative, it can give different relative results depending on the considered window size. For example, if we chose a one-hour window, then the absolute values of cross-correlation coefficients would be even greater. Our primary goal is to compare all considered events across all four data sources in order to determine the extents at which ULF waves can propagate to L-shells of different latitudes. We highlight cases which have cross-correlation r > 0.20 in all sources for a closer examination.

3. Results

We show all stages of the data analysis performed in this study on the substorm occurring on May 2, 2017, between 1000 and 1200 UTC. Fig. 6A shows the de-trended B_y component of the magnetic field measured by the ACE satellite. The solar wind speed during that time interval was ~450 km/s, which defines the delay in the effects on the ground due to the propagation from the L1 point of ~0.9 h. Thus, the

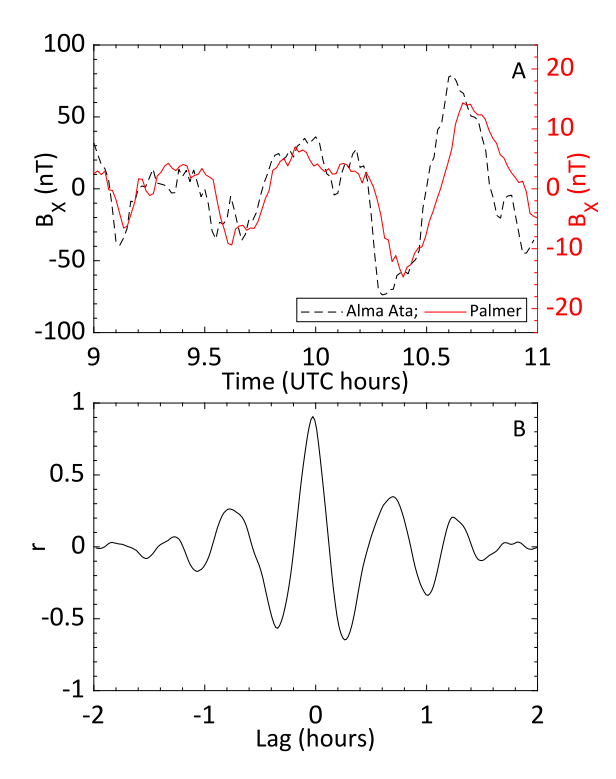


Fig. 5. (A) High-Frequency part (f > 0.30 mHz) of B_X of Alma Ata data (left axis) and that of B_X of Palmer data (right axis) on March 27, 2017. **(B)** Cross-Correlation coefficients of data in panel (A).

ACE magnetic field data is shifted in time by that delay. Fig. 6B shows relevant de-trended B_H measured at POKR station. Fig. 6C shows detrended B_x measured at PLMR station, and Fig. 6D shows de-trended B_x measured at AAA station. Fig. 6E, F, G, and H show the power spectral densities (PSDs) of the corresponding signals.

Fig. 6E shows that, during this event, the ACE satellite observed in the solar wind relatively large-amplitude ULF waves with frequencies of 0.30 mHz, 0.50–0.55 mHz, and 0.80 mHz, the first of which is an artificial peak since it is result of filtering with cut-off frequency 0.30 mHz as discussed above. Fig. 6F, G, and H show that the non-artificial dominant frequencies of the waves measured in high, middle and low latitudes are in the range of 0.50–0.55 mHz. These results suggest that the ULF waves detected in the solar wind may be related to the waves observed in high, mid, and low latitudes.

To verify this hypothesis, we calculate a correlation coefficient, r, between the signals detected in the solar wind and at the high-latitude POKR station. For example, Fig. 7A shows signals recorded at ACE and POKR, and Fig. 7C shows their cross-correlation. The cross-correlation function has a semi-periodic structure with a period close to the period of the observed waves. That indicates that the two considered signals have a similar frequency for at least one hour. The cross-correlation between the low-latitude and mid-latitude (AAA-PLMR), high-latitude and mid-latitude (POKR-PLMR), and low-latitude and high-latitude (AAA-POKR) stations has values of $r \sim 0.82$, $r \sim 0.77$, and $r \sim 0.85$, respectively, which are relatively large values. Fig. 7B shows that the signals from POKR and AAA have similar periods, although the magnitudes of these signals differ approximately by a factor of 6. For example, at 10.75 UTC, the maximum amplitude of the signal at AAA station is 80 nT, and the maximum amplitude of the signal at POKR station is 14 nT.

A summary of the analysis results of 75 events is presented in Table 1 (first 75 events). It shows that 28 events have a good match of dominant frequencies in power spectral density; 38 events have a cross-correlation of r > 0.2 of the detected waves across all sources;

and 17 events feature both a good match of dominant frequencies and a cross-correlation of r > 0.2 across all sources.

Except those events, there are also events with other outcomes. Fig. 8 shows a substorm event #58, in which high-latitude (POKR) and mid-latitude (PLMR) waves have the same dominant frequency of about 0.75 mHz, and high-latitude (POKR) waves have relatively large amplitude reaching 200 nT. Nonetheless, neither mid-latitude nor lowlatitude waves have relatively large amplitudes during the substorm (around 2-3 nT and 5-20 nT, respectively), implying that the ULF waves did not propagate to these latitudes. Among other examples, during the substorm event #13, the non-artificial dominant frequencies of ACE, POKR, and AAA are close, around 0.60-0.65 mHz, however the frequency of PLMR is 0.75 mHz and the cross-correlation coefficients are mostly very low (from 0.18 to 0.22, with only large coefficient of 0.51 between AAA and POKR). In other cases, such as event #14, there are relatively large cross-correlation coefficients across ground stations (0.42, 0.44, and 0.80), but different dominant frequencies (from 0.45 mHz to 0.75 mHz with only one match between ACE and AAA). Event #70 is noticeable by the same frequency of 0.45 mHz in all sources, however the cross-correlation coefficients are low (from 0.13

The results of the analysis of the nine GEM events are given in Table 1 (events # 76–84). They show that five events have similar dominant frequencies, five events have a good cross-correlation between signals from different sources, and four events have both. These observations of simultaneous enhancement of amplitudes of some particular frequencies and a good correlation between signals detected in the solar wind and at different latitudes on the ground suggest that these ULF waves may be produced by the same geophysical process.

Another interesting and noticeable feature in some of these events is the fact that the amplitude of the magnetic disturbances measured on the low-latitude AAA station is significantly larger than the amplitude of the magnetic disturbances measured at mid- and high-latitude stations. Possible explanation might be given by the fact that different regions of the magnetosphere can be distinguished by the excitation mechanisms. For example, waves in the high-latitude magnetic flux tubes are predominantly excited by processes in the magnetotail, gradients of plasmapause, processes in auroral and subauroral regions, which are detected by high-latitude stations (such as POKR). Low-latitude waves are mostly affected by the ring current and associated induced magnetic field, which are observed by low-latitude ground stations (such as AAA). Mid-latitude waves, being in the intermediate location between the former and the latter, can be affected by a combination of above-mentioned processes, and detected by mid-latitude stations (such as PLMR). In some cases, it turns out that the magnetic field induced by the ring current has the largest amplitude than that of detected at other latitudes. Such is the case shown in Fig. 6, where the waves at AAA have the largest amplitude at around 30 nT, whereas those at PLMR and POKR have around 2 nT and 5 nT, respectively.

The ring current dynamics is described by the geomagnetic Dst index. Fig. 9 shows plots of the Dst index and the velocity of the solar wind during September 29-October 1, 2012. This is the event #84 in Table 1. There are a few distinctive periods of solar wind acceleration towards the Earth. For example, at the daycount around 274.4 and 274.9, the solar wind speed increases by around 50 km/s and 100 km/s, respectively. These sudden changes are reflected on the Dst plot a little later, when the Dst index started to enhance. It should be mentioned here, that the expansion phase of the considered substorm (shaded rectangle on the plot) occurred during the increase of the Dst index, whereas the substorm recovery (around the daycount 275) was associated with the slightly increasing Dst index. Respectively for the two acceleration points, the index increased by about 50 nT starting at the daycount around 274.5, and by about 100 nT at the daycount 275. After the substorm, both solar wind speed and Dst started to decrease with almost the same pace. Even though these two parameters are not directly comparable, they show a good correlation between the rate of

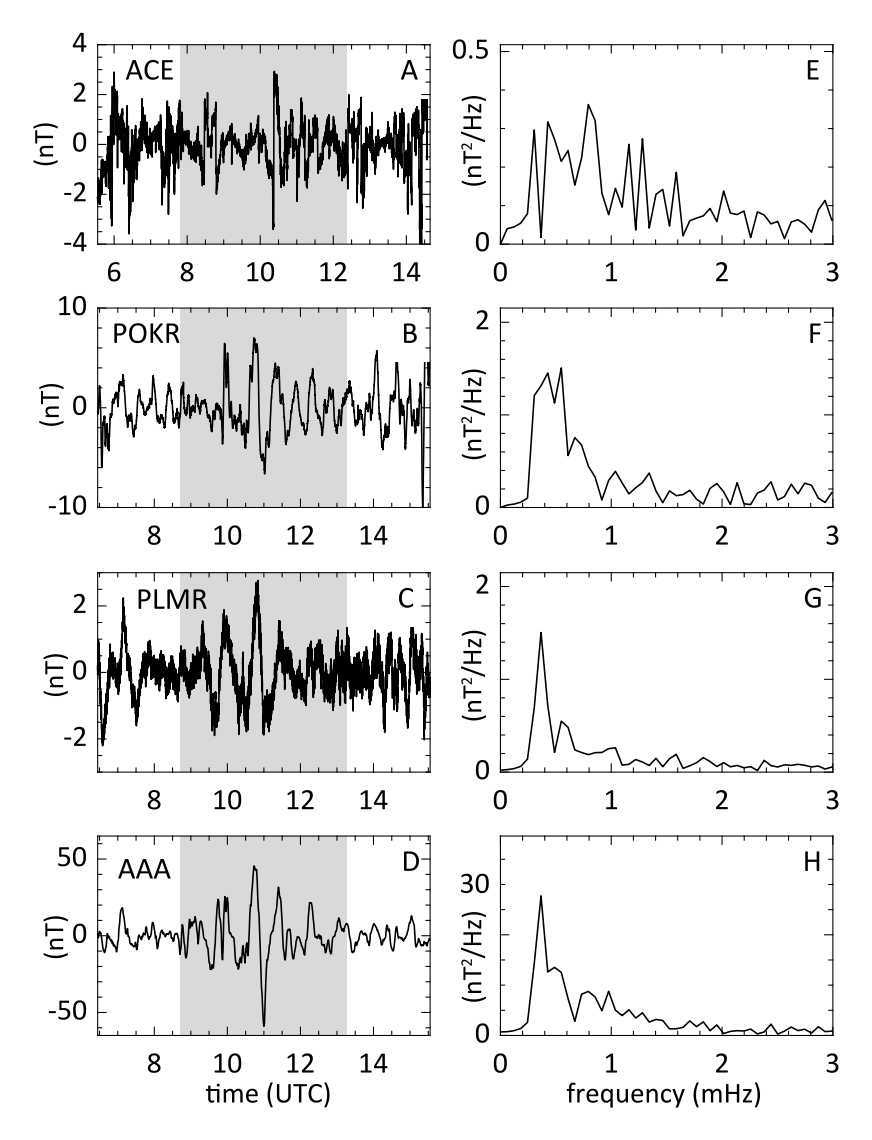


Fig. 6. Panes A, B, C, and D show the de-trended magnetic field data from ACE, POKR, PLMR, and AAA during the 05/02/2017 substorm. In particular, panel A shows de-trended B_y measured on the ACE satellite and shifted by 0.9 UTC according to the solar wind speed; panel B shows de-trended B_H from the POKR station; panel C shows de-trended B_X from the PLMR station; and panel D shows de-trended B_X from the AAA station. Shadowed rectangles indicate the time of the substorm. Panes E, F, G, and H show the power spectral densities of the corresponding magnetic fields calculated during the time of the substorm.

input of the magnetic field (via the solar wind) and the response of the Earth's inner magnetosphere.

Therefore, based on observations of total 84 events, we conclude that under some special conditions the ULF waves carried by the solar wind can drive the entire magnetosphere of the Earth and produce some detectable magnetic disturbances at high latitudes, mid latitudes, and low latitudes.

The last point of interest is the correspondence between the variations in the solar wind plasma density (or pressure) and the magnetic field fluctuations detected in the mid and low latitudes. To reveal this correspondence, we calculated PSD of the ion density fluctuations measured at ACE and a correlation coefficient between the fluctuations in the solar wind ion density and magnetic field measured on the ground. The results show that a correspondence between fluctuations in the solar wind ion density and the magnetic field measured on the ground is not as good as the correspondence between fluctuations in the magnetic field measured in the same locations. For example, the non-artificial dominant frequency of the ion density fluctuations is 0.75 mHz for the May 2, 2017, substorm event. It does not match the frequencies of the magnetic oscillations observed on the ground (0.50–0.55 mHz and 0.80 mHz). As for the cross-correlation, the ion density data are missing for four of the nine events. For existing events,

the magnitudes of cross-correlation between the ion density and the magnetic field measured at AAA station are typically lower than the values of the correlation coefficients calculated for the magnetic field data.

Fig. 10A shows the normalized distribution of non-artificial dominant frequencies in four analyzed data sources in all 84 events. The most frequently observed frequencies at all four sources are 0.45–0.55 mHz, and 0.80 mHz. A frequency of 0.50 mHz is the most common for high-latitude station (POKR), and low-latitude station (AAA), whereas the solar wind (ACE) and mid-latitude station (AAA) have values of 0.55 mHz and 0.45 mHz. All four sources share second most common frequencies of 0.75–0.80 mHz.

Fig. 10B shows the normalized distribution of non-artificial dominant frequencies during quiet times preceding the substorm events. It shows that the most common dominant frequencies for quiet events are 0.45–0.60 mHz and 0.75–0.80 mHz, which are quite close to those of substorm events described above. This means that those frequencies are generally present in the global resonator of the Earth's magnetosphere before and during the substorms. The amplitudes of waves with such frequencies are smaller in quiet periods, and they are increased during substorms.

Table 1 Summary of 84 observations from Poker Flat, Palmer, Alma Ata stations and the ACE satellite. Shaded cells indicate events with good correlation of spectral patterns. Asterisk indicates cases with cross-correlation r > 0.2 in all sources.

#	Date	Substorm time, UTC	Dominant frequencies (ACE, POKR, PLMR, AAA), mHz	Cross-Correlation Coefficients, r (ACE-POKR, AAA-PLMR, POKR-PLMR, AAA-POKR)		
1	10/9/15	1000 - 1400	0.80, 0.55, - , 0.45	0.30, -, -, 0.75		
2	11/4	1000 - 1400	0.60, 0.55, - , 0.80	0.32, -, -, 0.33		
3	11/7	0600 - 1000	0.50, 0.55, -, 0.60	0.38, -, -, 0.49		
1	12/6	1030 - 1400	0.55, 0.55, - , 0.75	0.31, -, -, 0.57		
5	12/14	1400 - 1800	0.50, 0.50, - , 0.50	0.15, -, -, 0.46		
5	12/20	1500 – 1800	0.90, 0.75, - , 0.55	0.24, -, -, 0.39		
7	01/20/16	1400 – 1800	0.65, 0.60, - , 0.80	0.22, -, -, 0.50		
3	01/24	1200 – 1600	0.80, 0.65, - , 0.55	0.27, -, -, 0.63		
.9	01/28	0800 - 1100	0.80, 0.45, 0.85, 0.50	0.56, 0.51, 0.53, 0.51		
.0	02/16	1600 – 1800	0.45, 0.45, 0.50, 0.60	0.30, 0.32, 0.27, 0.10		
1	02/17	1300 – 1600	0.65, 0.60, 0.50, 0.50	0.23, 0.35, 0.20, 0.35		
2						
	03/6	1600 – 1900	0.85, 0.45, 0.60, 0.60	0.19, 0.46, 0.20, 0.42		
:13	03/11	1300 – 1600	0.55, 0.45, 0.65, 0.65	0.44, 0.73, 0.33, 0.21		
:14	03/19	0800 – 1000	0.50, 0.75, 0.45, 0.50	0.52, 0.80, 0.44, 0.42		
5	04/13	1300 – 1600	0.60, 0.55, 0.50, -	0.38, -, 0.28, -		
:16	05/8	1500 - 1700	0.75, 0.50, 0.50, 0.55	0.25, 0.64, 0.29, 0.53		
7	07/14	0800 - 1100	0.75, 0.80, 0.45, 0.50	0.19, 0.43, 0.28, 0.29		
18	08/3	0900 - 1100	0.50, 0.60, 0.80, 0.50	0.34, 0.78, 0.60, 0.49		
:19	08/6	0900 - 1100	0.50, 0.60, 0.50, 0.45	0.54, 0.57, 0.48, 0.54		
20	09/27	0800 - 1100	0.45, 0.55, 0.45, 0.50	0.45, 0.32, 0.09, 0.36		
1	09/27	1200 – 1600	0.45, 0.80, 0.80, 0.55	0.34, 0.64, 0.12, 0.30		
22	09/28	900 – 1200	0.55, 0.65, 0.55, 0.60	0.39, 0.23, 0.36, 0.54		
23	09/28	1500 - 1700	0.50, 0.65, 0.45, 0.50	0.39, 0.65, 0.56, 0.42		
4	09/29	1400 - 1700	0.50, 0.55, 0.65, 0.50	0.18, 0.64, 0.40, 0.19		
25	09/30	800 – 1200	0.55, 0.55, 0.55, 0.65	0.54, 0.38, 0.43, 0.57		
26	10/2	1000 – 1400	0.45, 0.80, 0.55, 0.55	0.28, 0.23, 0.56, 0.56		
7	10/4	1200 – 1400	0.85, 0.50, 0.45, 0.50	0.32, 0.12, 0.16, 0.67		
:28						
	10/13	1100 – 1400	0.55, 0.55, 0.50, 0.45	0.47, 0.44, 0.49, 0.54		
9	10/13	1400 – 1800	0.60, 0.55, 0.75, 0.65	0.20, 0.55, 0.49, 0.52		
:30	10/14	700 – 1000	0.80, 0.75, 0.60, 0.65	0.31, 0.48, 0.65, 0.35		
51	10/17	900 – 1200	0.65, 0.60, 0.75, 0.65	0.18, 0.22, 0.19, 0.51		
52	10/24	1200 – 1400	0.85, 0.55, 0.60, 0.80	0.41, 0.35, 0.18, 0.33		
3	10/25	1200 - 1500	0.60, 0.65, 0.80, 0.50	0.15, 0.69, 0.22, 0.37		
4	10/25	1600 – 1900	0.50, 0.60, 0.45, 0.45	0.29, 0.46, 0.22, 0.20		
55	10/26	800 - 1100	0.55, 0.45, 0.75, 0.65	0.17, 0.64, 0.32, 0.12		
6	10/26	1300 - 1800	0.65, 0.55, 0.85, 0.65	0.18, 0.47, 0.45, 0.23		
7	10/27	800 - 1000	0.55, 0.55, 0.45, -	0.18, -, 0.38, -		
8	10/27	1100 - 1400	0.50, 0.65, 0.80, -	0.21, -, 0.16, -		
9	10/27	1400 - 1700	0.75, 0.60, 0.50, -	0.37, -, 0.57, -		
:40	10/28	900 - 1100	0.60, 0.55, 0.80, 0.60	0.23, 0.39, 0.35, 0.49		
41	10/29	400 - 800	0.55, 0.50, 0.45, 0.60	0.49, 0.44, 0.63, 0.41		
2	10/29	1200 - 1500	0.60, 0.50, 0.45, 0.60	0.24, 0.25, 0.48, 0.11		
- 3	10/30	1100 – 1400	0.65, 0.50, 0.50, -	0.26, -, 0.42, -		
:44	11/1	1000 – 1600	0.60, 0.65, 0.90, 0.50	0.33, 0.48, 0.27, 0.25		
45	11/2	1100 – 1600	0.75, 0.45, 0.45, 0.50	0.46, 0.45, 0.70, 0.51		
46	11/3	800 – 1000	0.50, 0.60, 0.55, 0.50	0.66, 0.57, 0.42, 0.69		
47	11/10	1300 – 1600	0.50, 0.55, 0.50, 0.60	0.30, 0.64, 0.29, 0.43		
48	11/12	1100 – 1300	0.60, 0.50, 0.60, 0.55	0.38, 0.69, 0.44, 0.54		
:49	02/16/17	1200 – 1600	0.45, 0.85, 0.50, 0.45	0.49, 0.52, 0.60, 0.68		
49 50	02/10/17	800 – 1000	0.45, 0.60, 0.60, 0.45			
				0.28, 0.43, 0.53, 0.22		
1	02/22	900 – 1200	0.45, 0.55, - 0.,55	0.18, -, -, 0.43		
52	02/24	1200 – 1600	0.60, 0.55, 0.45, 0.75	0.22, 0.21, 0.27, 0.51		
3	03/1	1000 – 1200	0.80, 0.50, 0.50, 0.55	0.28, 0.24, 0.34, 0.15		
4	03/2	1000 – 1200	0.80, 0.80, 0.55, 0.75	0.38, 0.38, 0.07, 0.73		
5	03/3	800 - 1000	0.55, 0.65, 0.60, -	0.21, -, 0.40, -		
6	03/3	900 - 1100	0.85, 0.60, 0.60, -	0.18, -, 0.05, -		
7	03/3	1500 - 1900	0.80, 0.65, 0.60, -	0.33, -, 0.40, -		
58	03/6	900 - 1200	0.55, 0.75, 0.75, 0.60	0.27, 0.46, 0.44, 0.33		
9	03/6	1300 - 1500	0.55, 0.55, 0.60, 0.50	0.16, 0.29, 0.21, 0.22		
:60	03/8	900 - 1100	0.55, 0.60, 0.60, 0.55	0.32, 0.51, 0.51, 0.52		
¢61	03/8	1100 – 1400	0.50, 0.75, 0.60, 0.60	0.30, 0.44, 0.68, 0.32		
	03/9	1200 – 1600	0.85, 0.50, 0.50, 0.65	0.32, 0.78, 0.46, 0.39		

(continued on next page)

Table 1 (continued).

±77 *78

*79

*80

*81

82

83

84

76

03/17/13

03/27/17

05/02/17

06/01/13

09/19/13

09/24/13

06/06/02

07/03/01

09/30/12

0.24, 0.55, 0.70, 0.61 0.35, 0.43, 0.33, 0.51 0.08, 0.31, 0.37, 0.27 0.40, 0.45, 0.43, 0.61 0.43, 0.91, 0.49, 0.49 0.36, 0.14, 0.14, 0.40 0.24, 0.67, 0.56, 0.77 0.13, 0.17, 0.50, 0.46 0.32, 0.76, 0.22, 0.13 0.07, 0.55, 0.72, 0.47 0.30, 0.57, 0.38, 0.52 0.13, 0.15, 0.42, 0.40

0.27, 0.42, 0.65, 0.61

0.27, 0.63, 0.34, 0.19 0.25, 0.76, 0.52, 0.47

0.29, 0.82, 0.77, 0.85

0.26, 0.41, 0.52, 0.31

0.46, 0.76, 0.36, 0.30

0.27, 0.25, 0.39, 0.26

0.39, -, -, -0.46, -, -, -

0.38, 0.72, 0.18, 0.49

,			
*63	03/10	900 – 1200	0.50, 0.55, 0.45, 0.45
*64	03/12	1200 - 1400	0.90, 0.75, 0.65, 0.60
65	03/21	1500 - 1900	0.55, 0.85, 0.75, 0.55
*66	03/22	800 - 1200	0.50, 0.90, 0.65, 0.45
*67	03/27	800 - 1200	0.75, 0.90, 0.65, 0.50
68	03/29	800 - 1000	0.60, 0.60, 0.45, 0.50
*69	03/31	800 - 1100	0.90, 0.80, 0.55, 0.50
70	04/4	800 - 1000	0.45, 0.45, 0.45, 0.45
71	04/20	800 - 1200	0.55, 0.90, 0.75, 0.55
72	04/22	900 - 1100	0.45, 0.75, 0.60, 0.80
*73	04/22	1200 - 1700	0.85, 0.60, 0.55, 0.50
74	04/23	800 - 1100	0.85, 0.80, 0.65, 0.55
*75	04/25	800 - 1100	0.80, 0.45, 0.90, 0.45

0900 - 1300

0900 - 1300

0900 - 1300

0400 - 0800

0600 - 1000

1000 - 1400

0700 - 1100

1200 - 1600

1500 - 1900

					Correlation coefficient, r				
2	POKR /	·	ACE	A				,	c
B _Y (nT)	مواللدو ود	Am /	$\frac{\sqrt{4}}{\sqrt{100}}$	ME		\sim	\triangle	$\setminus \wedge \wedge$	0
	AND AND		WW		= [\bigvee	V 0 .	
-2		70		-10					
10	10.5	11	11.5	12	-2	-1	0	1	2
50	· · · · · · · · · · · · · · · · · · ·			10 B	Γ.				$\frac{1}{D}$
	POKR	7	AAA	1	ţ	\wedge	/\		
B _X (nT)	\ \ \ \ \ \ \ \ \ \ \ \ \ \ \ \ \ \ \	1		∕્રા₀€		\sim / \setminus	///	\wedge	0
m× . √√	~~~~		V~	✓] å	<	V 1	\		
-50		\\\		1	-		V V		
10	10.5	11	11.5		-2	-1	0	1	
	ti	me (UTC)				tim	e lag (hou	ırs)	

0.55, 0.50, 0.55, 0.60

0.50, 0.90, 0.65, 0.50

0.80, 0.55, 0.55, 0.50

0.60, 0.55, 0.55, 0.50

0.85, 0.55, 0.50, 0.50

0.50, 0.50, 0.45, 0.80

0.45, 0.75, -, -

0.45, 0.65, -, -

0.75, 0.65, 0.90, 0.45

Fig. 7. (A) De-trended B_Y from the ACE satellite and B_H from the POKR station during 05/02/2017 substorm. (B) De-trended B_Y from the AAA station and B_H from the POKR station during 05/02/2017 substorm. (C) Correlation coefficient between signals shown in panel (A). (D) Correlation coefficient between signals shown in panel (B).

It is interesting to compare our results with the results presented in similar studies. For example, Mishin et al. (2002) analyzed frequencies of ULF waves detected by multiple sensors during the September 25, 1998, substorm. They found that the first two maxima of the power spectral density of the disturbances in the magnetic field occur at frequencies 0.80 mHz and 1.40 mHz. These frequencies correspond to the wave periods of 20 min and 12 min respectively (shown in Fig. 2 in their paper). We processed their data by the technique outlined in our paper and confirmed their results.

In total, waves with the frequency of 0.80 mHz are represented as non-artificial dominant ones in 22 out of 84 analyzed events. Waves with the frequency of 1.40 mHz appear in 24 events, however, their amplitude is comparable with the amplitude of the dominant wave only in seven events and it is less than the amplitude of the dominant wave in other events. Therefore, it is reasonable to conclude that the frequency of 0.80 mHz is indeed one of the main frequencies of ULF waves occurring during substorms. This conclusion is in the agreement with the results reported by Kepko et al. (2002), Viall et al. (2009), Marin et al. (2014) and Guido et al. (2014).

There are two important questions which need to be discussed in connection with the observations presented in the paper. The first question is the possible mechanism providing coupling between the

disturbances in the solar wind and the waves in mid and low latitudes. It is reasonable to assume that this coupling includes interaction between fast magnetosonic MHD modes propagating across the ambient magnetic field and shear Alfvén waves propagating along the magnetic field. A coupling between these two types of waves can be particularly efficient on the sharp transverse gradients in the plasma density. The sharp density gradients can also lead to a generation of the MHD surface waves, which can be coupled to the small-scale dispersive Alfvén waves (Hasegawa, 1976) and the fast MHD waves, and hence, to facilitate energy transfer from fast to shear MHD modes. In that sense, it is important to mention that all three L shells considered in our study can be associated with some transverse density gradients in the magnetosphere, as described in the beginning of the Data Sources and Analysis Methods section.

The second question is about a relatively large amplitude of the observed waves. This feature suggests that there is a resonance mechanism in the magnetosphere, which amplifies the waves standing in the resonator driven by the disturbances in the solar wind. There are two classical resonators in the magnetosphere-ionosphere system. The first one is the Field Line Resonator (FLR), formed by the entire closed magnetic flux tube bounded by the ionosphere (Cummings et al., 1969). The second is the Ionospheric Alfvén Resonator (IAR), formed by the ionospheric E region and a strong gradient in the Alfvén speed at

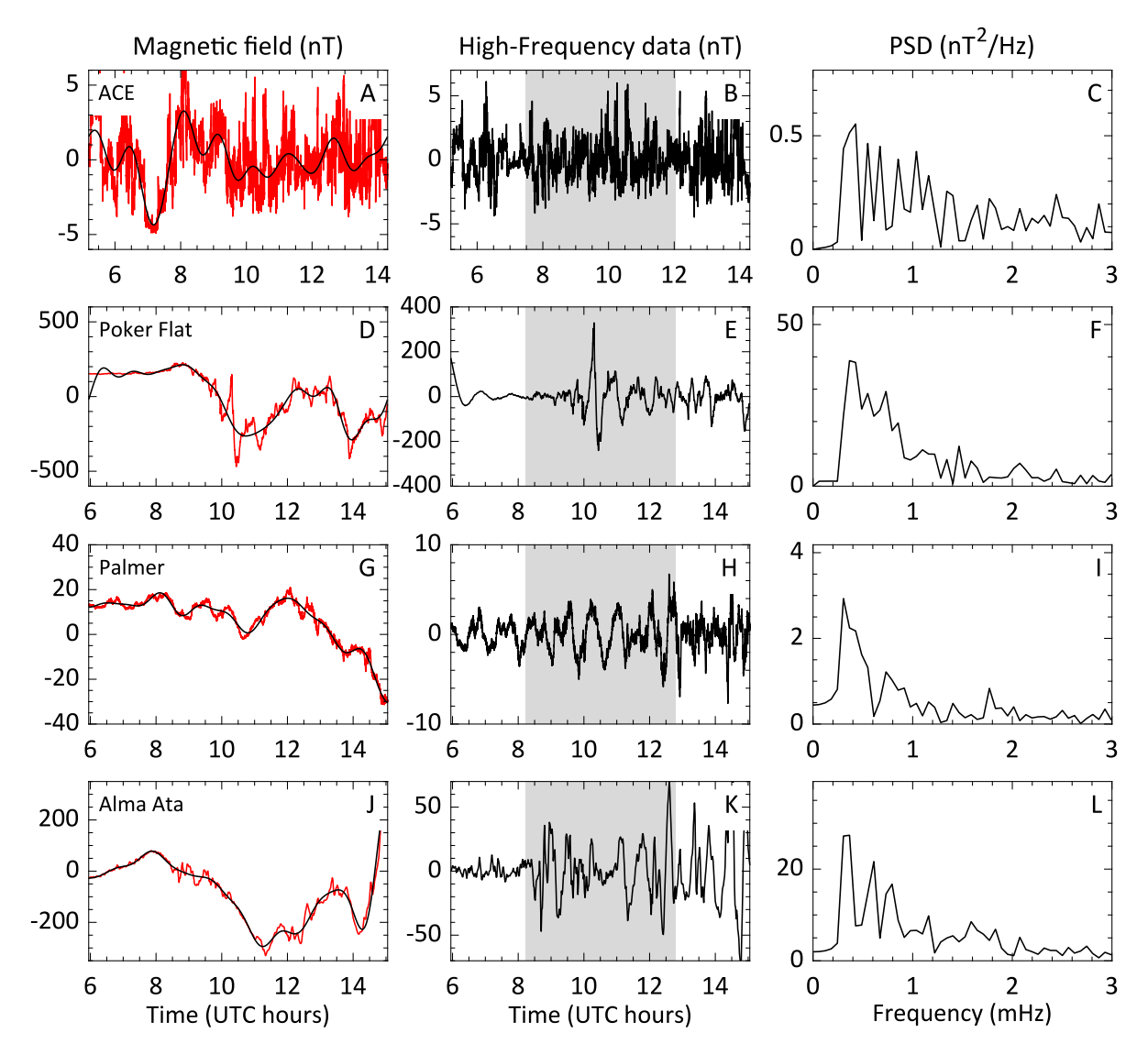


Fig. 8. Substorm event on March 6, 2017. **(A)** B_Y measured on ACE satellite. ACE data is shifted by 0.75 UTC according to the solar wind speed. **(B)** High-frequency part (f > 0.30 mHz) of B_Y on ACE satellite. Shaded region indicates substorm time. **(C)** Power Spectral Density (PSD) of data in panel (B) over 4 h period. **(D)** B_H measured on Poker Flat station. **(E)** High-frequency part of B_H on Poker Flat station. **(F)** PSD of data in panel (E) over 4 h period. **(G)** B_X measured on Palmer station. **(H)** High-frequency part of B_X on Palmer station. **(I)** PSD of data in panel (H) over 4 h period. **(J)** B_X measured on Alma Ata station. **(K)** High-frequency part of B_X on Alma Ata station. **(L)** PSD of data in panel (K) over 4 h period.

the altitude 0.5–1.0 R_E above the ground (Polyakov and O. Rapoport, 1981). At high latitudes, the lowest eigenfrequency of FLR can be \sim 0.9–1.0 mHz (Samson et al., 1992a; Fenrich et al., 1995), which is close to the frequencies observed in our study. The eigenfrequency of the IAR is normally much higher, \sim 0.1–1.0 Hz; therefore, this resonator cannot be used for amplification of the considered waves.

An important feature of the events selected at PLMR and AAA is that during the time interval when the large-amplitude waves were observed, the *Dst* index characterizing the behavior of the ring current has been disturbed as well. For example, Fig. 11A shows behavior of the *Dst* index during the time interval when the large-amplitude ULF waves (shown in Fig. 5A) were observed at Palmer and Alma Ata stations. The substorm occurred during the strong Dst index increase from about 20 to 50 nT. The Dst index increase occurred shortly after the solar wind speed increase from about 460 to 540 km/s started at around the daycount 86.2. Overall, the solar wind speed acts as if it is a precursor to the Dst index changes. Such conclusion about the correlation between the Dst index and solar wind speed during magnetically active times is also made by Huang et al. (2004). For example, starting from about daycount 86, both Dst index and solar

wind speed started to increase. Then, at around daycount 87.6, both of the parameters reached their local maximum, and finally started to decrease after the daycount 87. The solar wind dynamic pressure is proportional to the square of the solar wind speed, $p \sim nv^2$, where n is the solar wind plasma density. Thus, at least for this particular substorm on March 27, 2017, the solar wind dynamic pressure played a significant role in the substorm development.

In contrast, Fig. 11B shows that Dst index and solar wind speed have no correlation in the above-mentioned substrom event #58, on March 6, 2017, at 900–1200 UTC. For example, there is a sharp increase of the Dst index from about 13 nT to 33 nT at daycounts around 65.4 to 65.7. However, the solar wind speed during this time was gradually decreasing from about 600 km/s to 575 km/s. Overall, the Dst index experiences sharp changes during these 3 days of observation, whereas solar wind speed has a slowly decreasing trend.

A possible scenario which may explain the same frequencies of ULF waves observed in the solar wind and mid and low latitudes is that disturbances of the magnetic field and plasma pressure in the solar wind directly modulate the dynamics of the reconnection in the tail. That, in turn, impose these modulations on the FLR at high latitude and on the

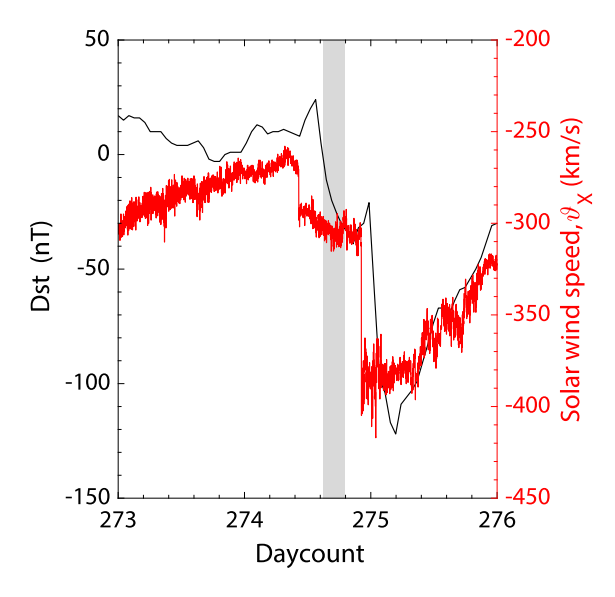


Fig. 9. Dst index and the x component (in the direction from the Earth towards the Sun) of the solar wind speed. The shaded rectangular marks the time of the substorm event occurred on 09/30/2012 at 1500-1900 UTC.

dynamic of the ring current in the plasmasphere. The amplitude of the ULF wave oscillations at high latitude (usually between 100-500 nT) is much larger than that at mid and low latitudes (5–15 nT, and 20-100 nT, respectively). Oscillations of the ring current generate ULF waves detected on the ground at high and mid latitudes. This scenario will be investigated with 3D numerical simulations of the MHD model, which we plan to do next.

4. Conclusions

The paper presents results of the data analysis of 84 intense substorm events. Data used in this study are from the ACE satellite taken measurements in the solar wind and ground magnetometers at high (L = 5.76), middle (L = 2.46), and low (L = 1.87) latitudes. We estimated correlations between fluctuations of the magnetic field measured at all sources and correlations between fluctuations of the solar wind ion density and the magnetic field at high, middle, and low latitudes. The main conclusion is that the dominant frequencies of oscillations of the magnetic field are in the range of 0.45-0.80 mHz across all the sources, and 0.45-0.55 mHz are the most common ones across all sources. Among 84 events, 33 events have a good match of dominant frequencies in power spectral density; 43 events have a crosscorrelation of r > 0.2 of the detected waves across all sources; and 22 events feature both. Also, seven out of the nine GEM events have a strong correlation between the variation of the solar wind speed and the Dst index. Therefore, the results suggest that the variations of the magnetic field in the solar wind are one of the main drivers of the ULF magnetic field pulsations with frequencies less than 1 mHz detected in three different latitudes during substorms. The novelty of this paper is that it is among the first studies that investigate the ULF waves in the solar wind and at high, middle and low latitudes on the ground. It also shows that in the amplitude of the ULF waves observed at low latitudes is higher compare with the amplitude of ULF waves detected at middle latitudes. This feature suggests that these waves are generated by the disturbances in the ring current, which are driven by the disturbances of the magnetic field in the solar wind. The coupling between the solar wind and the inner magnetosphere of the Earth can occur at the night side and on the day side of the Earth. The exact mechanism of coupling between the oscillations in the solar wind and the magnetic pulsations detected in these parts of the magnetosphere is the subject of future numerical studies.

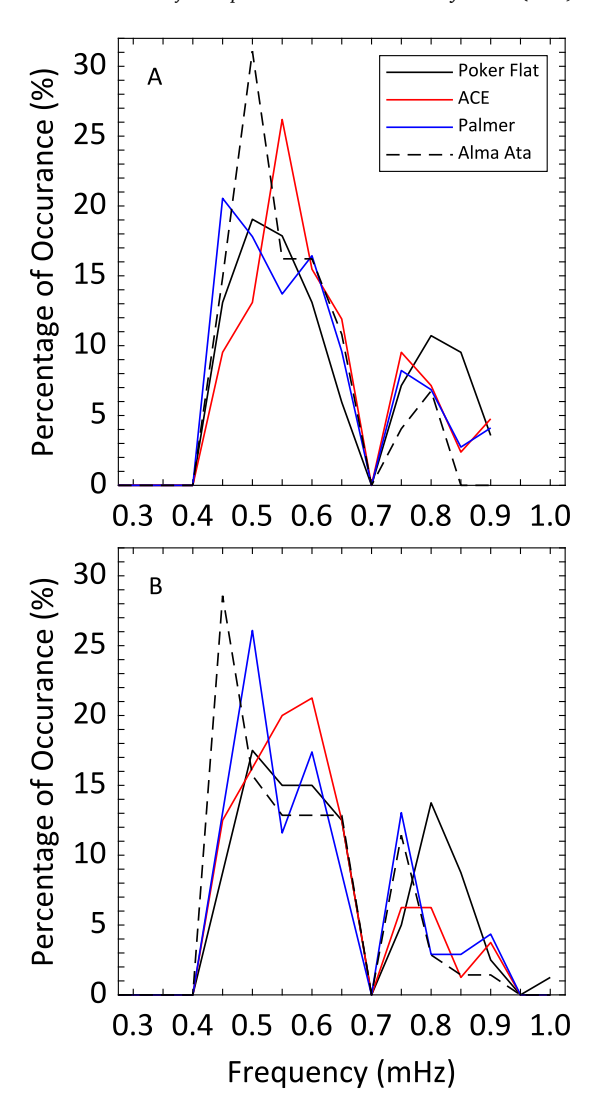


Fig. 10. (A) Distribution of dominant frequencies in ACE, Poker Flat, Palmer, and Alma Ata data during substorm events. (B) Distribution of dominant frequencies in ACE, Poker Flat, Palmer, and Alma Ata data during quiet times preceding the substorm events in (A).

CRediT authorship contribution statement

Mergen Alimaganbetov: Data curation, Formal analysis, Visualization, Writing - original draft. Anatoly V. Streltsov: Conceptualization, Methodology, Writing - review & editing, Validation.

Acknowledgments

The research was supported by the National Science Foundation, USA award AGS 1803702. AE indices data are taken from http://wdc.kugi.kyoto-u.ac.jp/aedir/index.html. ACE magnetic field and solar wind parameters data were taken from http://www.srl.caltech.edu/ACE/ASC/. Poker Flat magnetometer data were taken from http://www.gi.alaska.edu/magnetometer/. Palmer magnetometer data were taken from http://magnetometers.bc.edu/. Alma Ata magnetometer data were taken from http://ionos.kz/?q=ru/geomagdata. The list of nine GEM events was taken from ULF wave modeling challenge at https://gem.epss.ucla.edu/mediawiki/index.php/FG:_ULF_Wave_Modeling,_Effects,_and_Applications.

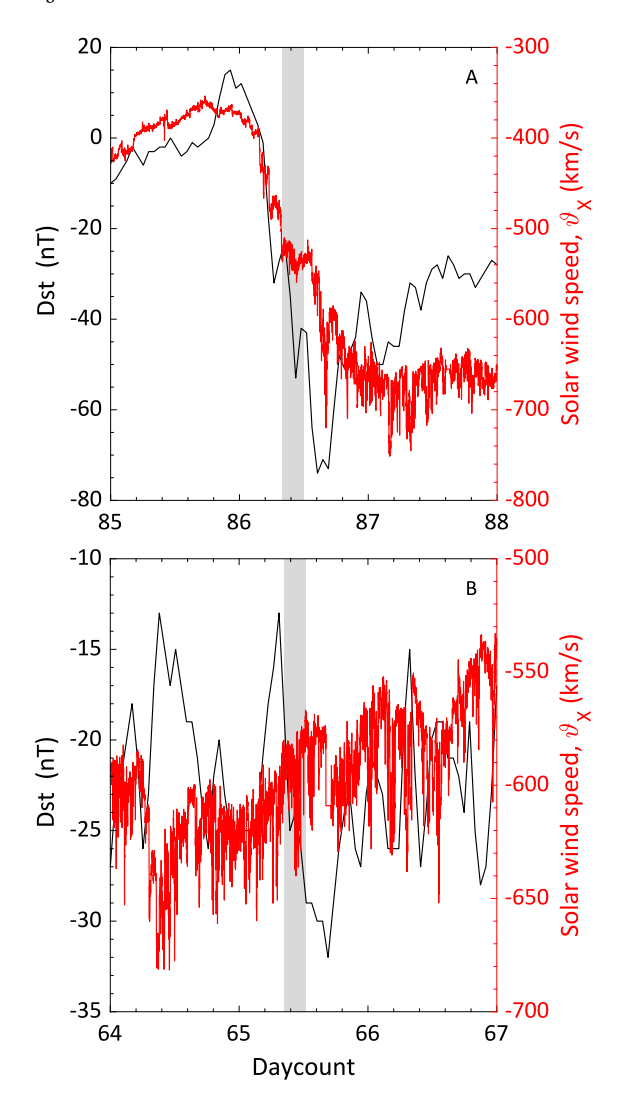


Fig. 11. (A) Dst index and solar wind speed on March 26–28, 2017. A shaded region indicates the March 27, 2017, substorm at 800–1200 UTC. (B) Dst index and solar wind speed on March 5–7, 2017. A shaded region indicates the March 6, 2017, substorm at 900–1200 UTC.

Source: Adapted from http://wdc.kugi.kyoto-u.ac.jp/dst_realtime/ and http://www.srl.caltech.edu/ACE/ASC/.

References

Alimaganbetov, M., Streltsov, A.V., 2018. ULF waves observed during substorms in the solar wind and on the ground. J. Atmos. Sol.-Terr. Phys. 181 (April), 10–18. http://dx.doi.org/10.1016/j.jastp.2018.10.007.

Angelopoulos, V., Chapman, J.A., Mozer, F.S., Scudder, J.D., Russell, C.T., Tsuruda, K., Mukai, T., Hughes, T.J., Yumoto, K., 2002. Plasma sheet electromagnetic power generation and its dissipation along auroral field lines. J. Geophys. Res.: Space Phys. 107 (A8), 1–20. http://dx.doi.org/10.1029/2001JA900136.

Atkinson, G., 1970. Auroral arcs: Result of the interaction of a dynamic magnetosphere with the ionosphere. J. Geophys. Res. (1896–1977) 75 (25), 4746–4755. http://dx.doi.org/10.1029/JA075i025p04746.

Boyd, A.J., Spence, H.E., Claudepierre, S.G., Fennell, J.F., Blake, J.B., Baker, D.N., Reeves, G.D., Turner, D.L., 2014. Quantifying the radiation belt seed population in the 17 March 2013 electron acceleration event. Geophys. Res. Lett. 41 (7), 2275–2281. http://dx.doi.org/10.1002/2014GL059626.

Cravens, T.E., 1997. Physics of Solar System Plasmas. Cambridge University Press, p. 71. http://dx.doi.org/10.1017/CBO9780511529467.

Cummings, W.D., O'Sullivan, R.J., Coleman, P.J., 1969. Standing Alfvén waves in the magnetosphere. J. Geophys. Res. 74 (3), 778–793. http://dx.doi.org/10.1029/ ia074i003p00778.

Fenrich, F.R., Samson, J.C., Superdarn, N., 1995. ULF high- and low-m field line resonances observed with the Super Dual Auroral Radar Network a source disturbance in the magnetosphere generates Data Analysis Goose. J. Geophys. Res. 100 (A11), 21,535–21,547. http://dx.doi.org/10.1029/95JA02024.

Foster, J.C., Erickson, P.J., Baker, D.N., Claudepierre, S.G., Kletzing, C.A., Kurth, W., Reeves, G.D., Thaller, S.A., Spence, H.E., Shprits, Y.Y., Wygant, J.R., 2014a. Prompt energization of relativistic and highly relativistic electrons during a substorm interval: Van Allen Probes observations. Geophys. Res. Lett. 41 (1), 20–25. http: //dx.doi.org/10.1002/2013GI.058438.

Foster, J.C., Erickson, P.J., Coster, A.J., Thaller, S., Tao, J., Wygant, J.R., Bonnell, J.W., 2014b. Storm time observations of plasmasphere erosion flux in the magnetosphere and ionosphere. Geophys. Res. Lett. 41 (3), 762–768. http://dx.doi.org/10.1002/ 2013GI.059124.

Galinsky, V.L., Sonnerup, B.U.Ö., 1994. Dynamics of shear velocity layer with bent magnetic field lines. Geophys. Res. Lett. 21 (20), 2247–2250. http://dx.doi.org/10. 1029/94GL01706

Guido, T., Tulegenov, B., Streltsov, A.V., 2014. Large-amplitude ULF waves at high latitudes. J. Atmos. Sol.-Terr. Phys. 119, 102–109. http://dx.doi.org/10.1016/j. jastp.2014.07.006.

Hasegawa, A., 1976. Particle acceleration by MHD surface wave and formation of aurora. J. Geophys. Res. (1896–1977) 81 (28), 5083–5090. http://dx.doi.org/10. 1029/JA081i028p05083.

Huang, C.S., Foster, J.C., Goncharenko, L.P., Reeves, G.D., Chau, J.L., Yumoto, K., Kitamura, K., 2004. Variations of low-latitude geomagnetic fields and Dst index caused by magnetospheric substorms. J. Geophys. Res.: Space Phys. 109 (A5), http://dx.doi.org/10.1029/2003JA010334.

Kepko, L., Spence, H., 2001. Periodicity in the solar wind as a source of ULF pulsations. In: AGU Fall Meeting Abstracts.

Kepko, L., Spence, H.E., Singer, H.J., 2002. ULF waves in the solar wind as direct drivers of magnetospheric pulsations. Geophys. Res. Lett. 29 (8), 39–1–39–4. http://dx.doi.org/10.1029/2001GL014405.

Li, Z., Hudson, M., Patel, M., Wiltberger, M., Boyd, A., Turner, D., 2017. ULF wave analysis and radial diffusion calculation using a global MHD model for the 17 March 2013 and 2015 storms. J. Geophys. Res.: Space Phys. 122 (7), 7353–7363. http://dx.doi.org/10.1002/2016JA023846.

Mann, I.R., O'Brien, T.P., Milling, D.K., 2004. Correlations between ULF wave power, solar wind speed, and relativistic electron flux in the magnetosphere: solar cycle dependence. J. Atmos. Sol.-Terr. Phys. 66 (2), 187–198. http://dx.doi.org/10.1016/j.jastp.2003.10.002.

Mann, I.R., Ozeke, L.G., Murphy, K.R., Claudepierre, S.G., Turner, D.L., Baker, D.N., Rae, I.J., Kale, A., Milling, D.K., Boyd, A.J., Spence, H.E., Reeves, G.D., Singer, H.J., Dimitrakoudis, S., Daglis, I.A., Honary, F., 2016. Explaining the dynamics of the ultra-relativistic third Van Allen radiation belt. Nat. Phys. 12, 978, https://doi.org/10.1038/nphys3799.

Marin, J., Pilipenko, V., Kozyreva, O., Stepanova, M., Engebretson, M., Vega, P., Zesta, E., 2014. Global Pc5 pulsations during strong magnetic storms: Excitation mechanisms and equatorward expansion. Ann. Geophys. 32 (4), 319–331. http://dx.doi.org/10.5194/angeo-32-319-2014.

Mishin, E.V., Foster, J.C., Potekhin, A.P., Rich, F.J., Schlegel, K., Yumoto, K., Taran, V.I., Ruohoniemi, J.M., Friedel, R., 2002. Global ULF disturbances during a stormtime substorm on 25 September 1998. J. Geophys. Res.: Space Phys. 107 (A12), 1–11. http://dx.doi.org/10.1029/2002JA009302.

Miura, A., 1996. Stabilization of the Kelvin-Helmholtz instability by the transverse magnetic field in the Magnetosphere-Ionosphere Coupling System. Geophys. Res. Lett. 23 (7), 761–764. http://dx.doi.org/10.1029/96GL00598.

Moore, T., Nykyri, K., Dimmock, A., 2016. Cross-scale energy transport in space plasmas. Nat. Phys. 12, http://dx.doi.org/10.1038/nphys3869.

Nykyri, K., Otto, A., Lavraud, B., Mouikis, C., Kistler, L.M., Balogh, A., Rème, H., 2006. Cluster observations of reconnection due to the Kelvin–Helmholtz instability at the dawnside magnetospheric flank. Ann. Geophys. 24 (10), 2619–2643. http://dx.doi.org/10.5194/angeo-24-2619-2006.

Pilipenko, V.A., Kozyreva, O.V., Engebretson, M.J., Detrick, D.L., Samsonov, S.N., 2002. Dynamics of long-period magnetic activity and energetic particle precipitation during the May 15, 1997 storm. J. Atmos. Sol.-Terr. Phys. 64 (7), 831–843. http://dx.doi.org/10.1016/S1364-6826(02)00074-3.

Polyakov, S., O. Rapoport, V., 1981. The ionospheric Alfvén resonator. Geomagn. Aeronomy/Geomagn. Aeron. 21, 816–822.

Rae, I.J., Mann, I.R., Murphy, K.R., Ozeke, L.G., Milling, D.K., Chan, A.A., Elkington, S.R., Honary, F., 2012. Ground-based magnetometer determination of in situ Pc4–5 ULF electric field wave spectra as a function of solar wind speed. J. Geophys. Res.: Space Phys. 117 (A4), http://dx.doi.org/10.1029/2011JA017335.

Russell, A.J.B., Wright, A.N., Streltsov, A.V., 2013. Production of small-scale Alfvén waves by ionospheric depletion, nonlinear magnetosphere-ionosphere coupling and phase mixing. J. Geophys. Res.: Space Phys. 118 (4), 1450–1460. http://dx.doi.org/10.1002/jgra.50168, arXiv:1302.3158.

Samson, J.C., Harrold, B.G., Ruohoniemi, J.M., Greenwald, R.A., Walker, A.D., 1992a. Field line resonances associated with MHD waveguides in the magnetosphere. Geophys. Res. Lett. 19 (5), 441–444. http://dx.doi.org/10.1029/92GL00116.

Samson, J.C., Wallis, D.D., Hughes, T.J., Creutzberg, F., Ruohoniemi, J.M., Greenwald, R.a., 1992b. Substorm intensifications and field line resonances in the nightside magnetosphere. J. Geophys. Res. 97, 8495. http://dx.doi.org/10.1029/91.JA03156.

Sato, T., 1978. A theory of quiet auroral arcs. J. Geophys. Res.: Space Phys. 83 (A3), 1042–1048. http://dx.doi.org/10.1029/JA083iA03p01042.

- Shprits, Y.Y., Subbotin, D., Drozdov, A., Usanova, M.E., Kellerman, A., Orlova, K., Baker, D.N., Turner, D.L., Kim, K.C., 2013. Unusual stable trapping of the ultrarelativistic electrons in the Van Allen radiation belts. Nat. Phys. 9, 699, https://doi.org/10.1038/nphys2760.
- Streltsov, A.V., Pedersen, T.R., Mishin, E.V., Snyder, A.L., 2010. Ionospheric feedback instability and substorm development. J. Geophys. Res.: Space Phys. 115 (A7), n/a–n/a. http://dx.doi.org/10.1029/2009JA014961.
- Takahashi, K., Ohtani, S.i., Hughes, W.J., Anderson, R.R., 2001. Correction to "CRRES observation of Pi2 pulsations: Wave mode inside and outside the plasmasphere" by K. Takahashi et al. J. Geophys. Res. 106, 29945. http://dx.doi.org/10.1029/2001.JA000259.
- Takahashi, N., Seki, K., Teramoto, M., Fok, M.C., Zheng, Y., Matsuoka, A., Higashio, N., Shiokawa, K., Baishev, D., Yoshikawa, A., Nagatsuma, T., 2018. Global distribution of ULF waves during magnetic storms: Comparison of arase, ground observations, and BATSRUS + CRCM simulation. Geophys. Res. Lett. 45 (18), 9390–9397. http://dx.doi.org/10.1029/2018GL078857.
- Trakhtengertz, V., Feldstein, A., 1984. Quiet auroral arcs: Ionosphere effect of magnetospheric convection stratification. Planet. Space Sci. 32 (2), 127–134. http://dx.doi.org/10.1016/0032-0633(84)90147-8.

- Turner, D.L., Angelopoulos, V., Morley, S.K., Henderson, M.G., Reeves, G.D., Li, W., Baker, D.N., Huang, C.L., Boyd, A., Spence, H.E., Claudepierre, S.G., Blake, J.B., Rodriguez, J.V., 2014. On the cause and extent of outer radiation belt losses during the 30 September 2012 dropout event. J. Geophys. Res.: Space Phys. 119 (3), 1530–1540. http://dx.doi.org/10.1002/2013JA019446.
- Verkhoglyadova, O.P., Tsurutani, B.T., Mannucci, A.J., Mlynczak, M.G., Hunt, L.A., Paxton, L.J., Komjathy, A., 2016. Solar wind driving of ionosphere-thermosphere responses in three storms near St. Patrick's Day in 2012, 2013, and 2015. J. Geophys. Res.: Space Phys. 121 (9), 8900–8923. http://dx.doi.org/10.1002/2016JA022883.
- Viall, N.M., Kepko, L., Spence, H.E., 2009. Relative occurrence rates and connection of discrete frequency oscillations in the solar wind density and dayside magnetosphere. J. Geophys. Res.: Space Phys. 114 (1), 1–10. http://dx.doi.org/10.1029/ 2008JA013334.
- Zou, S., Ridley, A., Jia, X., Boyd, E., Nicolls, M., Coster, A., Thomas, E., Ruohoniemi, J.M., 2017. PFISR observation of intense ion upflow fluxes associated with an SED during the 1 June 2013 geomagnetic storm. J. Geophys. Res.: Space Phys. 122 (2), 2589–2604. http://dx.doi.org/10.1002/2016JA023697.